The effect of the chemical distribution on the mechanical properties of the Al-5.5wt%Si-5wt%Zn-0.2wt%Mg alloy after thixoforging and solution heat treatment

Gabriela Lujan Brollo[1], Cecília Tereza Weishaupt Proni[1], Eugênio José Zoqui[1]

[1]Departamento de Engenharia de Manufatura e Materiais - DEMM/FEM/Unicamp, Rua Mendeleyev, 200, CEP 13083-860, Campinas, SP, Brazil.
e-mail: gbrollo@fem.unicamp.br, wyliah@gmail.com, zoqui@fem.unicamp.br

ABSTRACT

The effect of heat and strain during the semisolid processing route on the microstructural evolution and mechanical performance of the Al-5.5wt%Si-5wt%Zn-0.2wt%Mg alloy was evaluated. The as cast alloy was heated and partially melted to 588 °C (fs = 0.40), thixoformed (in an open die forged) and solution heat-treated (SHT) at 525 °C for 1 to 6 h. The microstructural evolution and chemical distribution (SEM-EDS) of the main alloying elements were evaluated at each step of the processing route. The SHT for 2.5 h after thixoforming showed to be adequate considering (a) the spheroidization of Si crystals, (b) the formation of Fe- and Mn-rich platelet-like particles in the eutectic phase, (c) the Mg dissolution from the Mg_2Si conglomerates and (d) the homogeneous Zn diffusion along the entire part. As a consequence of the higher circularity of secondary particles, the possibility of crack formation and propagation under stress was minimized. The possible formation of solute clusters and GP zones containing Zn, Mg, Si and Cu was enabled due to the dissolution and diffusion of secondary elements during SHT, which increased the alloy's mechanical strength. Larger Si crystals and the homogeneous spatial spread of Zn resulted in the hardness increase of the SHT alloy.

Keywords: thixoforming, Al-Si-Zn-Mg alloys, solution heat treatment, solid solution strengthening.

1. INTRODUCTION

The benefits provided by the precipitation hardenable aluminum alloys can be associated to the advantages of the semisolid materials (SSM) processing, promoting new possibilities of production routes with an improved mechanical performance of the final product as presented in the work of KILICLI *et al.* [1], GECU *et al.* [2], CURLE [3], BINESH *et al.* [4], ROGAL [5] and CHEN *et al.* [6]. The demand for a rise in potential thixoformable alloys represents a technologic challenge in the field, encouraging research of new chemical systems and heat treatment routes after forming in the semisolid state.

Aluminum-silicon alloys (4xxx series) are broadly used in thixoforming operations. Silicon raises fluidity, reduces contraction during cooling and, at low contents, improves machinability. However, Si decreases the ductility as presented by ZOQUI [7]. On the other hand, alloys from series 7xxx, containing the combination of zinc and magnesium, present high impact resistance and tensile strength and excellent ductility. Al-Zn-Mg alloys belong to the group of Al alloys that presents mechanical strength similar to the structural steels, due to the formation of hardening particles along the matrix after precipitation heat treatment. Some of these precipitates are also responsible for the improvement in the corrosion resistance as well as fatigue and creep responses of these alloys as attested by SHIN *et al.* [8], GUO *et al.* [9], LIN *et al.* [10], LIN *et al.* [11], CHAO *et al.* [12], LEI *et al.* [13], WEN *et al.* [14], ABD EL-SALAM *et al.* [15], NADA *et al.* [16], and BAI, *et al.* [17].

Note that, several alloys from the Al-Si-Mg, Al-Si-Zn and Al-Zn-Mg tertiary systems are successfully used as thixoforming feedstock as presented by ZOQUI [7]. However, the simultaneous combination of these elements (the quaternary Al-Si-Zn-Mg system) for SSM processing applications was barely studied and represents a potential range of feedstock that combines the advantages of the thixoforming process with the possibility of heat treatment after forming for improved mechanical performance as presented by PRONI *et al.* [18], PRONI *et al.* [19] and DANTAS *et al.* [20]. Second phase particles found in precipitation hardenable Al-alloys are classified in three categories:

(1) Constituent precipitates with high melting point, thus not affected by solution heat treatment (SHT). These particles are usually coarse (ranging from 1-30 μm) and located at the primary phase grain boundaries, such as the Si,Fe-rich phases AlFeSi-β, Al_7Cu_2Fe, Mg_2Si, etc.;

(2) Dispersoid phases distributed along the primary phase matrix, extremely refined (approx. 0.5-2.0 μm) and also soluble only in the liquid, such as $Al_{12}Mg_2Cr$ and $Al_{18}Mg_3Cr_2$-E. Dispersoid particles perform a major role in hindering dislocations and sub-grain and grain boundaries migration, thus influencing recovery, primary and secondary recrystallization;

(3) Hardenable precipitates presenting lower melting point, such as $MgZn_2$-η, Al_2CuMg-S, $Al_2Mg_3Zn_3$-T and $CuMgAl_2$ phases. These particles are formed through ageing of the supersaturated Al-matrix as follows: α-supersaturated solid solution (α-ssss) → solute clusters → GP zones → metastable phases (e.g., *η'' and η'*) → stable phase (e.g., *η*).The solute clusters are aggregates of solute atoms (fully coherent with the Al matrix) and evolve rapidly into metastable precipitates during artificial aging. GP zones involve early stage precipitation (larger and more stable coherent solute aggregates with spherical morphology). Fine metastable precipitates transformed from GP zones are the main responsible for the hardening effect. If evolved to equilibrium phases with further aging, the coarse precipitates promote poorer hardening. The thermo-mechanical route as well as the chemical proportion of the alloying elements present in the alloy directly affect the size, morphology, amount and distribution of these particles as attested by KILICLI *et al.* [1], GECU *et al.* [2], CURLE [3], BINESH *et al.* [4], ROGAL [5] and CHEN *et al.* [6], SHU *et al.* [21], PRIYA *et al.* [22], AFSHARI *et al.* [23], ROMETSCH *et al.* [24], CHEN *et al.* [25] and ZHU *et al.* [26]. The presence of Zn in Al alloys plays a major role in the partitioning of Mg, Si, and Cu atoms from the Al matrix into solute clusters, GP zones and metastable precipitates, which results in a remarkable age hardening effect when compared to Zn-free alloys as attested by ZHU *et al.* [27], GUO *et al.* [28], and LIU *et al.* [29].

In this work, theAl-5.5wt%Si-5wt%Zn-0.2wt%Mg alloy is studied. Its thermodynamic stability, microstructural evolution during partial melting and rheological behavior under compression in the semisolid state were successfully evaluated in a previous studies by PRONI *et al.* [18], PRONI *et al.* [19] and DANTAS *et al.* [20]. Here the mechanical performance (tensile test and hardness) of this alloy will be evaluated as a response to the distribution and combination of its alloying elements and how these features are affected by strain (thixoforming operation) and heat (SHT) imposed to the alloy.

2. MATERIALS AND METHODS

The chemical composition of the Al-5.5wt%Si-5wt%Zn-0.2wt%Mgalloy, refereed here as Al5.5Si5Zn0.2Mg, was determined with an Anacom BILL-OES optical emission spectrometer and is shown in Table 1.

Table 1: Chemical composition of the Al5.5Si5Zn0.2Mg alloy.

Element	Si	Zn	Fe	Mg	Cu	Mn	Al
Wt.%[1]	5.5 ± 0.1	4.9 ± 0.3	0.24 ± 0.02	0.197	0.117	0.082	Bal.[2]

[1] When not indicated, maximum standard deviation is ± 0.005.[2] Balance.

CALPHAD simulation via Thermo-Calc® software was used to produce the diagram at thermodynamic equilibrium for the studied alloy in the temperature range of 0 to 700 °C (Fig. 1). The Si content of 5.5 wt% is shown as a white vertical line in the diagram. Compositions corresponding to the white areas lie outside the scope of this work. Phase transformations corresponding to colored areas are described at the right of the diagram. The following phases are formed during solidification at equilibrium: Liquidus occurs at 615 °C, with the formation of a pure face centered cubic Al matrix (Al_{FCC}) followed by the fcc Al-rich solid solution (Al-α), Si-rich eutectic and the Fe-rich AlFeSi-β phase, marking the solidus at 562 °C. In the solid state, the following compounds are expected to be formed: Al_8FeMg_3, Mg_2Si, Al_5Cu_2Mg, $MgZn_2$, Al_2Cu, $A3_{HCP}$ and $A1_{FCC}$, where A3 is a hexagonal compact phase formed by the combination of Zn and Cu with an approx. stoichiometry of $CuZn_{11}$ and A1 is a face centered cubic phase containing Si and Fe, with an approx. stoichiometry of Fe_5Si_2. As can be seen, Al, Si and Fe tend to combine at higher temperatures, forming secondary phases still in the semisolid condition. At lower temperatures, in the fully solid condition, the combination of other elements, such as Mg, Cu and Zn, also occurs.

The Thermo-Calc® software was also used to produce the liquid fraction (f_l) versus temperature (T) curve (Fig. 2) for the studied alloy so that the target temperature and liquid fraction for the semisolid characterization and processing could be determined. The following phases are formed during solidification at the Scheil condition: Liquidus occurs at 615 °C, with the formation of a pure face centred cubic Al matrix (Al_{FCC}) followed by the fcc Al-rich solid solution (Al-α), Si-rich eutectic (knee at 566 °C), the Fe-rich AlFeSi-β phase, the $Al_8FeMg_3Si_6$ and Mg_2Si compounds, marking the solidus at 495 °C. As can be seen, besides the Si-rich eutectic and the AlFeSi-β phase (already predicted at equilibrium), other Al,Fe,Mg,Si-rich secondary phases are formed in the semisolid state at the non-equilibrium of Scheil. The elements Zn and Cu remain in solid solution during the entire solidification interval.
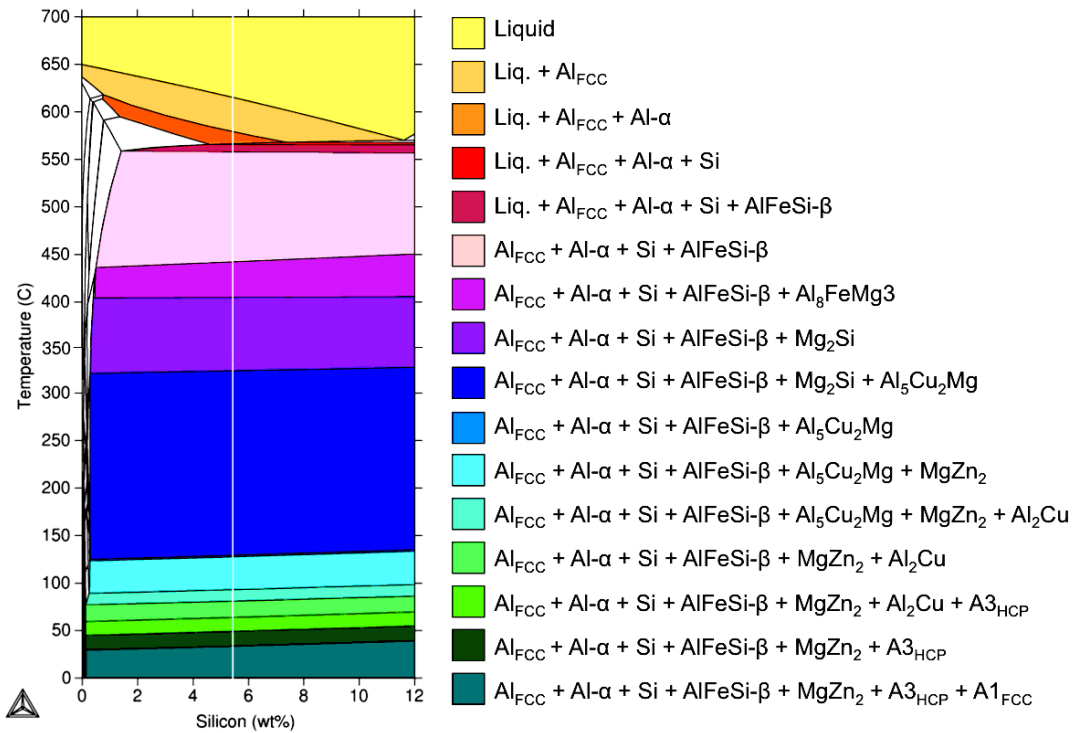
Figure 1: Phase diagram at thermodynamic equilibrium for the Al5.5Si5Zn0.2Mg alloy obtained via Thermo-Calc® simulation.
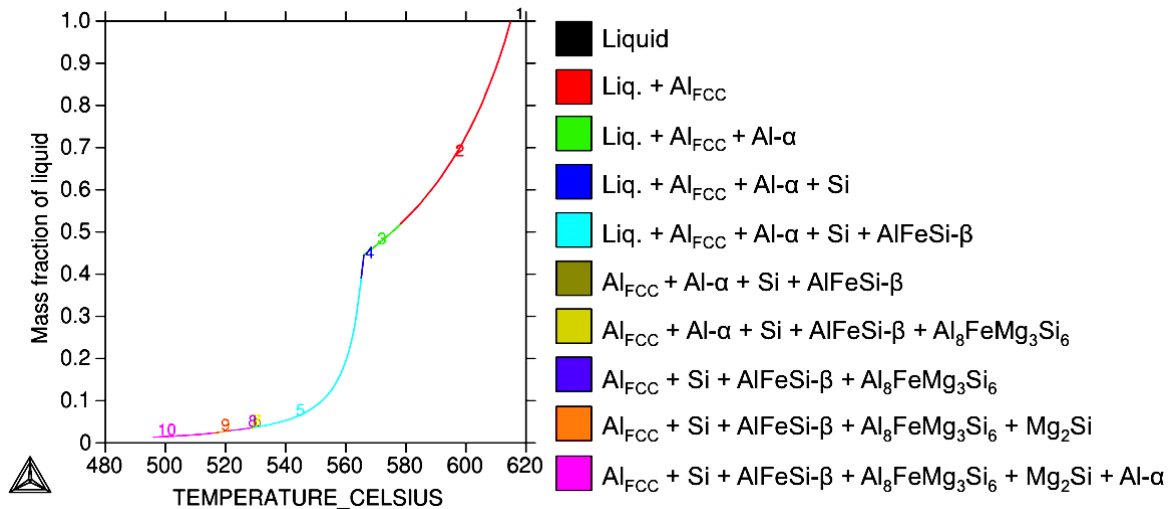

Figure 2: Liquid fraction vs. temperature curve for the Al5.5Si5Zn0.2Mg alloy during solidification at the Scheil condition obtained via Thermo-Calc® simulation.

The difference achieved in the solidus temperature between the phase diagram, Ts = 562 °C (Fig. 1), and the liquid fraction curve, Ts = 495 °C (Fig. 2), is due to the thermodynamic conditions assumed in the simulation for each case: the first predicts the phase transformations occurring at thermodynamic equilibrium; the second uses the non-equilibrium Scheil condition to predict the phase transformations. The Scheil model assumes that (1) no diffusion occurs in solid phases once they are formed, (2) infinitely fast diffusion occurs in the liquid at all temperatures by virtue of a high diffusion coefficient, thermal convection, Marangoni convection, etc., (3) equilibrium exists at the solid-liquid interface, and so compositions from the phase diagram are valid and (4) solidus and liquidus are straight segments. The Scheil model is generally used due to its higher accuracy when compared to real conditions.

The processing window was defined as ranging from T_{SSMI} = 567°C (above the eutectic knee) to T_{SSMF} = 612°C (below liquidus, with a security margin to prevent total melting). The target temperature for processing at which 0.40 fraction solid is present in the alloy is T_P= 588 °C. This temperature was chosen for the partial melting and thixoforming operation. The sensitivity at this temperature is df_l/dT = 0.009 °C^{-1}, a value far below the recommended by LIU *et al.* [29] with a maximum limit of 0.03 °C^{-1}.

The alloy was melted in a conventional furnace and poured 70 °C above $T_{liquidus}$ into a refrigerated copper mold (30 mm D, 220 mm L) with a 25 l/min water flow. During solidification in the refrigerated mold, the alloy was mechanically vibrated using an eccentric shaft (mechanical hammer) with amplitude of 0.7 mm, frequency of 10 kHz and acceleration ranging from 1.59 to 2.46 m s^{-2} to break up the dendritic solid. To maximize gas liberation, high purity argon was injected through the molten metal at 710 °C for 5 min before casting.

The as cast alloy was heated at 50 °C/min as in PRONI and ZOQUI [30] until it partially melted at 588 °C in an 8 kHz 20 kW Norax induction furnace and was immediately water quenched to characterize the morphological evolution of the alloy in the semisolid state. The samples used for this purpose were cylinders (30 mm D x 30 mm H) taken from the longitudinal segment of the as cast ingots. During heating, a thermocouple was inserted in a hole machined in the geometrical center of the sample (at the center of the flat surface of the cylinder, 4 mm D X 10 mm H).

Thixoforming via open-die forging was performed at the same conditions as the partial melting cycles, using an instrumented mechanical press that also works as a compression rheometer. The thixoforming samples were cylinders (30 mm D x 70 mm H) taken from the longitudinal segment of the as cast ingots, submitted to mechanical forming until a strain of 0.4-0.5 was achieved. Figure 3 shows an assembly of light optical micrographs taken at regular lengths of the radial section (center to border as 1 to 6; top to bottom as A to E) of an open-die thixoforged disk of the studied alloy. The distribution of the second phase is homogeneous throughout the part and the shape of the primary phase grains is globular and also homogeneous.
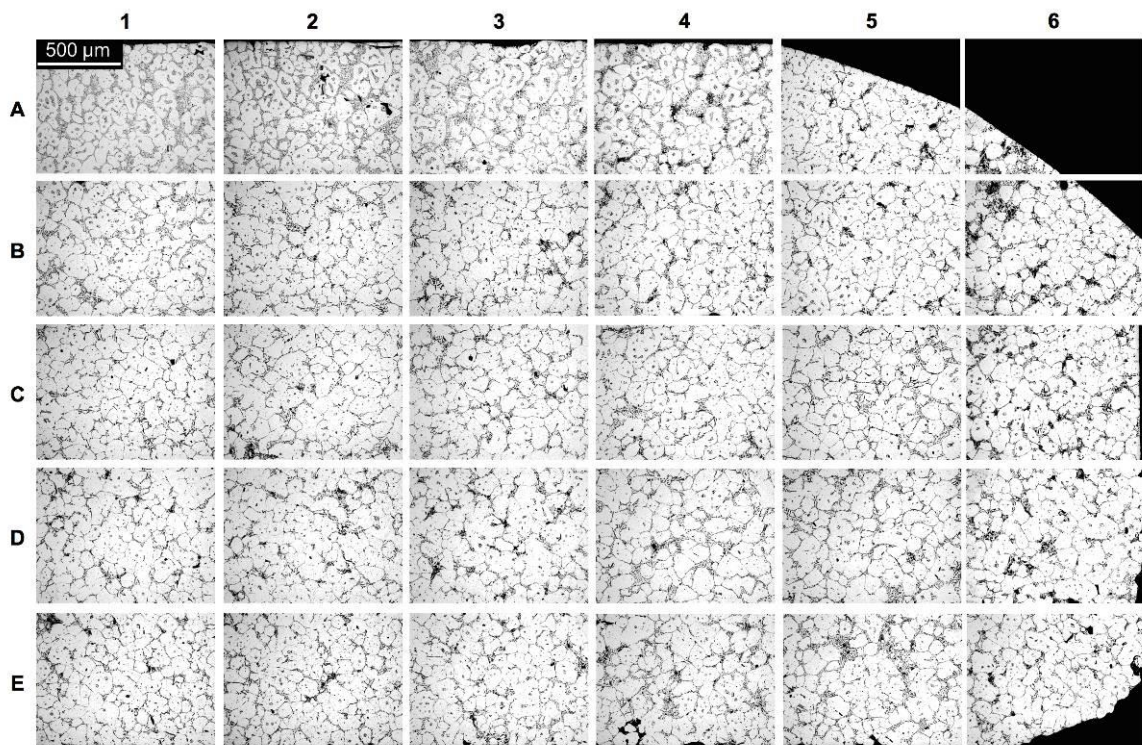

Figure 3: Micrographs assembly of the radial section (center to border - @ 1 to 6, and top to bottom - @ A to E) of an open die thixoforged disk (588 °C, ε = 0.5) of the Al5.5Si5Zn0.2Mg alloy.

The bulging aspect observed at the external edge of the samples (micrographs A-5 and A,B,E-6 in Fig. 3) are due to the following factors: (1) the use of an open die for the experiment, which allows the material to flow freely in the radial direction when compressed, without any physical restraint; (2) the high (momentaneous) apparent viscosity presented by the thixotropic fluid (semisolid metal) under high internal shearing stress (caused by the applied compressive stress) facilitates the sample´s structure collapse under the force of gravity. This factor explains mainly the large bulging at the top of the sample (micrographs A-5 and

A,B-6); (3) finally, the surface tension generated by the liquid phase in the semisolid metal leads to the formation of a stretched elastic membrane-like surface at the metal-air interface. This factor explains the smaller bulging at the bottom of the sample (micrograph E-6).

Solution heat treatment after thixoforming was performed in a resistive furnace at 10 °C/min to 525 °C, which is the temperature used for SHT of the A355 alloy (Al-5.0Si). Several holding times (1 to 6 h) were tested to achieve an optimal microstructure. After the elapsed time the samples were immediately water quenched.

Tensile tests were performed in a universal testing machine (MTS, model 810, 100 kN capacity load cell) connected to the Test Star II system, with initial velocity of 1.2 mm/min. The standard ASTM E8-16a (ASTM International E8-16a) [31] was chosen for the machining of the tensile test samples (6.0 ± 0.1 mm D, 30 mm A, 6 mm R, 24.0±0.1 mm G). Six replies were tested for each condition, which were as cast (AC), thixoforged (TF) and solution heat-treated (SHT) at 10 °C/min to 525 °C and 2.5 h of holding time.

Hardness Vickers measurements were performed in a Future Tech FV-800 equipment using 1 kgf load applied for 10 s on the base of the tensile test samples that presented results near the average behavior under tensile stress for each processing condition. Ten indentations were performed in each sample.

The microstructure for all the tested conditions was characterized by light optical microscopy (LOM), providing conventional black and white (B&W) images and polarized-light color micrographs, both using a Leica DM ILM equipment. For color microscopy, the samples were etched electrolytically in 1.8% Barker solution at 27 V for 180 s under stirring. Polarizing filters were used to obtain color images of the grains so that grains with the same crystal orientation had similar colorings. Each primary phase observed separately in a conventional B&W micrograph is referred to here as a "globule". It is assumed that adjacent globules with the same coloring in a polarized optical micrograph possess the same interconnected "skeleton" structure in three dimensions (3D). This structure is in turn represented by the grain observed in the two-dimensional (2D) images. A complete explanation of the relationship between grain and globule can be found in ZOQUI *et al.* [32].

Grain size (G_S) and globule size (GL_S) were determined using the Heyn intercept method (ASTM International E112-13) [33] applied to the LOM images. The phases and chemical distribution in the alloy were identified using secondary electron (SE), backscattered electron (BSE), and energy-dispersive spectroscopy (EDS) scanning electron microscopy (SEM). Binary images from the fractured surface of the tensile test samples were achieved using the threshold function using Image-J® 1.40 g software. The eutectic particles size (P_S), circularity, fraction (P_F) and planar density (P_D) were also calculated using the Image-J® 1.40 g software. P_s was considered to be the maximum Feret diameter. This is the normal distance between two parallel tangents touching the particle outline and is also known as the maximum caliper diameter. The shape factor (circularity, C) was calculated using the equation $C = (4\pi A)/P^2$, where A is the area and P the perimeter ($C = 1$: sphere; $C \to 0$: needle). P_F was estimated as the ratio of the area occupied by these particles to the total area of the respective LOM images. Finally, P_D was considered as the number of particles per $100 \times 100~\mu m^2$ of the LOM images.

3. RESULTS AND DISCUSSION

3.1 Effect of the SHT on the thixoformed microstructure

Figure 4 presents the microstructure of the Al5.5Si5Zn0.2Mg alloy as cast (AC, a and b), after partial melting at 50 °C/min to 588 °C ($f_s = 0.40$) followed by water quenching (PM, c and d), after thixoforming at $\varepsilon = 0.5$ (TF, e and f) and after the SHT at 525 °C ($f_s = 0.96$) for 2.5 h followed by water quenching (SHT, g and h). The micrographs highlight grains (Fig. 4, left – polarized LOM) and globules/silicon crystals (Fig. 4, right – B&W LOM).

Grains and globules are visibly enhanced (finer and globular) after partial melting (Fig. 4.c/d) when compared to the as cast condition (Fig. 4.a/b), which shows the effectiveness of controlled heating and partial melting as a feedstock preparation for this alloy. Silicon crystals become acicular and coarse after thixoforming (Fig. 4.e/f), when compared to the partially melted condition (Fig. 4.c/d), due to their solidification under shear while the alloy was being compressed between the dies. Thus, a SHT at 10 °C/min to 525 °C was applied to the alloy in order to achieve a better morphology for these particles in the final product. The holding time for the SHT presented in Fig. 4.g/h is 2.5 h (the choice for this particular holding time will be discussed ahead in this paper).

Figure 5 presents the microstructure of the Al5.5Si5Zn0.2Mg alloy after thixoforming at 588 °C until a strain of 0.5 (TF, left column: a, d, g and j) and the same region of the sample after the SHT at 525 °C (SHT, middle and right columns) for 1 (b, c), 2 (e, f), 3 (h, i) and 6 h (k, l) of holding time. The micrographs highlight grains (Fig. 5, right – polarized LOM) and eutectic particles (Fig. 5, left and middle – B&W LOM),

which are represented mainly by silicon crystals (dark grey) and, in lesser content, by Fe-rich precipitates (light grey).The eutectic particles size (P_s), circularity (C), fraction (P_F) and planar density (P_D, number of particles per 100x100 µm^2) are presented in Table 2.

The shape of the primary phase grains is progressively rounded with the increase in holding time from 1 to 6h. Grain size is visibly reduced from 1 to 3 h of SHT, due to the prominence of Ostwald ripening over coalescence, increasing again for 6 h, indicating severe coalescence.

As a general trend, with the progress of SHT from 1 to 6 h, the eutectic particles become coarser (rise in P_S in Table 2), rounder (rise in C) and heterogeneously distributed along the material (decrease in P_D). Furthermore, some constituent elements of these particles seem to diffuse from the second phase to the matrix, since it is observed a decrease in their area fraction (P_F) for longer SHT holding times. The rounding of Si crystals tips is more effective after 2 h of heating (Fig. 5.e). After 3 h (Fig. 5.h), the crystals become coarse and heterogeneously distributed in the matrix, forming clusters in concentrated regions around grain boundaries, which is detrimental to the mechanical properties under tensile stress and to further machining operations. Fragmentation and spheroidization followed by coarsening of Si crystals with the progression of SHT was previously observed for Al-Si-(Cu,Mg) alloys by BEROUAL, *et. al.* [34].
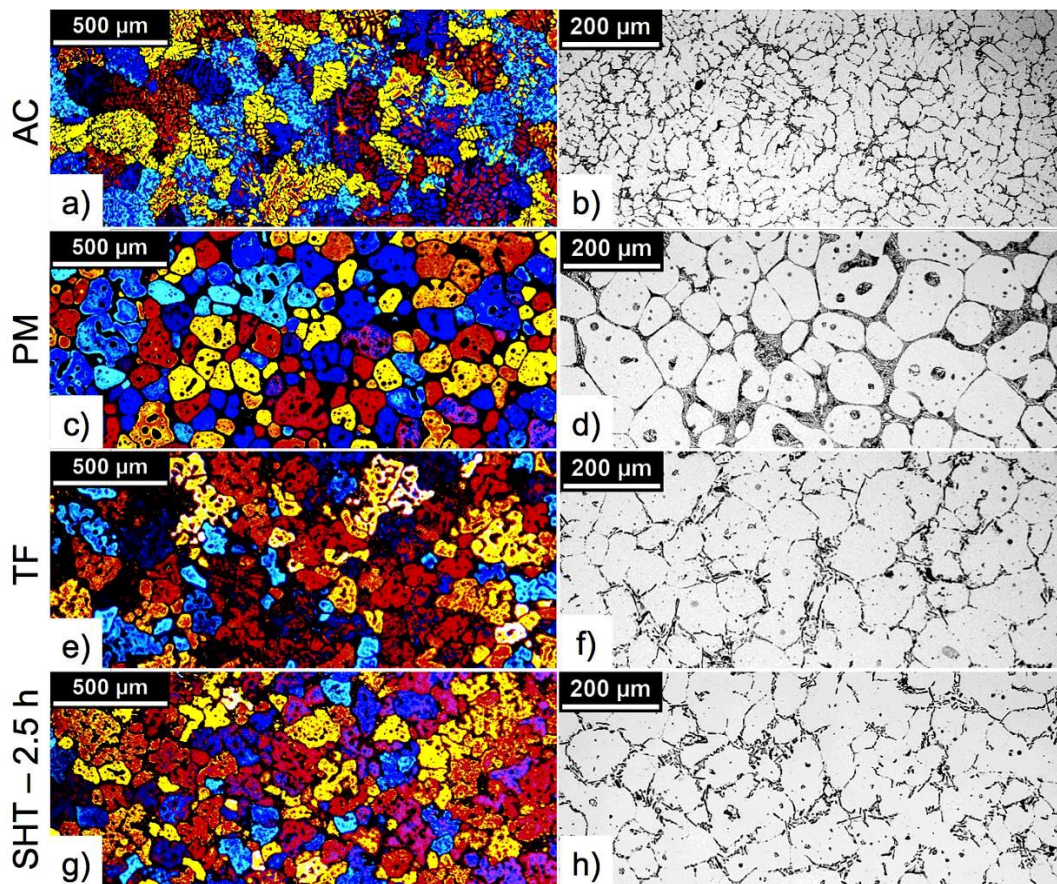

Figure 4: Micrographs highlighting grains (left) and globules/Si crystals (right) for the Al-5.5Si-5Zn-0.2Mg alloy as cast, AC (a/b), after partial melting at 50 °C/min to 588 °C (f_s = 0.40) followed by water quenching, PM (c/d), after thixoforming at 0.5 strain, TF (e/f), and after SHT at 525 °C for 2.5 h followed by water quenching (g/h).

Combining the reduction in grain size and an acceptable roundness, size and distribution of Si crystals, the ideal holding time should lie between 2 and 3 h. For this reason, an additional cycle of 2.5 h was performed and resulted in the best microstructure amongst the tested conditions (shown earlier in Fig. 4.g/h). The holding time of 2.5 h was then chosen for the following experiments in this work.
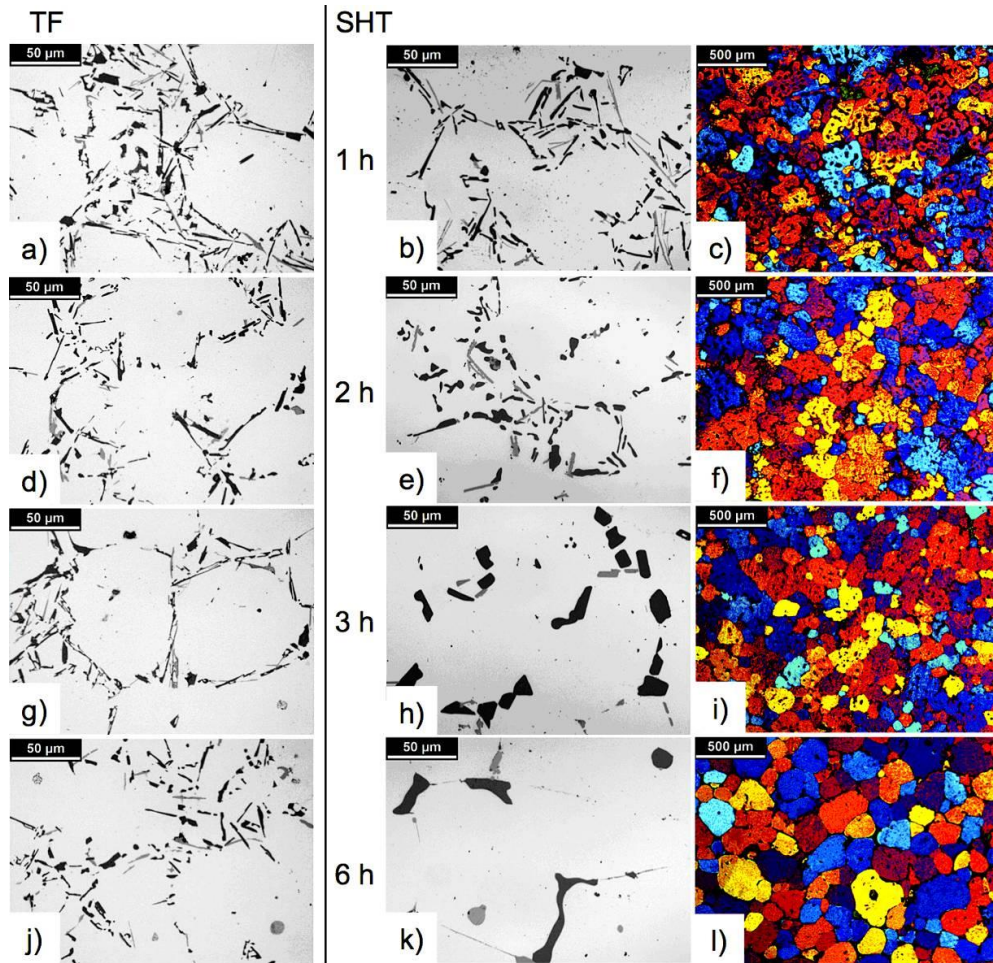
Figure 5: Micrographs highlighting globules and silicon crystals (left and middle) and grains (right) for the Al-5.5Si-5Zn-0.2Mg alloy after thixoforming at 588 °C until a strain of 0.5 (TF, left) and after SHT at 525 °C (middle and right) for 1 (a), 2 (b), 3 (c) and 6 h (d) of holding time.

Table 2: Microstructural parameters (average ± standard deviation) of eutectic particles for the Al-5.5Si-5Zn-0.2Mg alloy after thixoforming at 588 °C and SHT at 525 °C for 1 to 6 h of holding time.

CONDITION	P_S (µm)	CIRCULARITY	P_F (%)	P_D[1]
Thixoforged	10 ± 1	0.47 ± 0.06	8 ± 2	41 ± 7
SHT - 1 h	10 ± 2	0.52 ± 0.05	10 ± 2	43 ± 5
SHT - 2 h	9 ± 1	0.58 ± 0.05	8 ± 2	32 ± 6
SHT - 3 h	12 ± 1	0.64 ± 0.06	9 ± 2	12 ± 5
SHT - 6 h	13 ± 2	0.62 ± 0.03	5 ± 2	6 ± 5

[1]Average number of eutectic particles per 100x100 µm^2.

3.2 Effect of the SHT on the Mechanical Performance

Table 3 presents the tensile test parameters, as well as the hardness Vickers measurements for the tensile test samples of the Al5.5Si5Zn0.2Mg alloy. Also, the grain and globule size for the alloy as cast, partially melted, thixoformed and SH treated for 2.5 h are presented. Figure 6 shows the data from table 2 as a bar graph for the as cast, thixoformed and SHT conditions. Data from the partially melted condition is not shown in Fig. 6 because it is not a final processing condition, so its microstructural and mechanical characterization are only a reference to evaluate the efficacy of the feedstock preparation for the SSM processing.

The SHT treated alloy presents the best mechanical performance amongst the analyzed conditions. Considering the standard deviations of the measurements, the SHT and the as cast conditions are equally strength. The thixoformed condition is slightly inferior to both, probably due to grain fragmentation, acicular shape of the eutectic Si crystals and localized residual stress originated during forming, which facilitated crack generation and propagation. Furthermore, the hardness and ductility of the SHT samples are superior to the as cast and thixoformed conditions. The SHT promoted a rise of 6 % in σ_e, 4 % in σ_u, 13 % in ε_u and 8.5

% in HV when compared to the thixoforged material.

Confronting the mechanical performance data with the microstructural evolution (section 3.1) results in a surprising controversy: the SHT sample presented the largest grain size and also the higher mechanical strength and hardness. It is expected that the extensive diffusion during SHT enlarges the grain in comparison to the thixoformed condition (rise of 7.1 % in G_S), but it is well known that this behavior should be detrimental to the alloy strength. It is known that diffusion during SHT also promotes residual stress relief and spheroidization, which probably contributed to the ductility improvement observed for this condition in comparison to the others.

Table 3: Average ± standard deviation for Yield Stress (σ_e), Ultimate Tensile Stress (σ_u) and Strain (ε_u) and Hardness Vickers for the tensile test samples of the Al5.5Si5Zn0.2Mg alloy. Grain (G_S) and globule size (GL_S) for the studied alloy as cast, partially melted, thixoformed and SHT for 2.5 h are also shown.

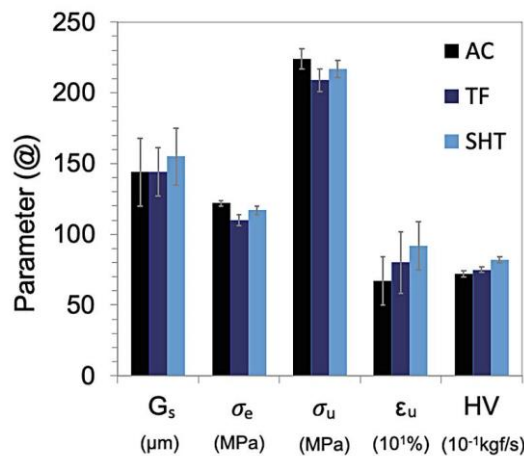| CONDITION	G_S (µm)	GL_S (µm)	σ_e (MPa)	σ_u (MPa)	ε_u (%)	HV (10^{-1}kgf/s)
AC	144 ± 24	-	122 ± 2	224 ± 7	6.7 ± 1.7	72 ± 2
PM	137 ± 19	100 ± 11	-	-	-	66 ± 2
TF	144 ± 17	113 ± 12	110 ± 4	209 ± 8	8.0 ± 2.2	75 ± 2
SHT - 2.5 h	155 ± 20	90 ± 9	117 ± 3	217 ± 6	9.2 ± 1.7	82 ± 2

Figure 6: Comparative analysis of mechanical and microstructural parameters for the Al5.5Si5Zn0.2Mg alloy in the as cast (AC) condition, after thixoforging (TF) at 588 °C (strain = 0.5) and after SHT at 525 °C for 2.5 h.

Figure 7 shows fractography images (obtained via SEM in a/b and filtered as binary images in c/d) and the plane perpendicular to the fractured surface (via LOM in e/f) of the tensile test samples of the Al-5.5Si-5Zn-0.2Mg alloy after thixoforming at 588 °C (a, c, e) and after SHT for 2.5 h at 525 °C (b, d, f). Features inside the circles in Fig. 7.a/b are zoomed-in at the top of the figure.

The fracture behavior of Al-Si-Cu-(Mg,Zn) alloys depends on a conjoint effect of the physical nature of second phases, local stress and temperature and the intrinsic nature of the matrix as observed by GAO *et al.* [35]. Brittle Fe- and Si-rich eutectic crystals are extensively found in the primary-phase grain boundary for the tested conditions. These stress-concentrating precipitates are present in several regions of the fractured surface of the samples (black arrows in Fig. 7.a/b) along with cleavage facets (yellow arrows in Fig. 7.a/b). Micro-cracks (blue circles 1 to 6 in Fig. 7.a/b), river-like patterns (red circles 7 to 9 in Fig. 7.a/b) and terrace-like stairs (green rectangles in Fig. 7.a/b), usually associated to crack initiation and propagation from the grain boundary, are also present in the fractured surfaces.
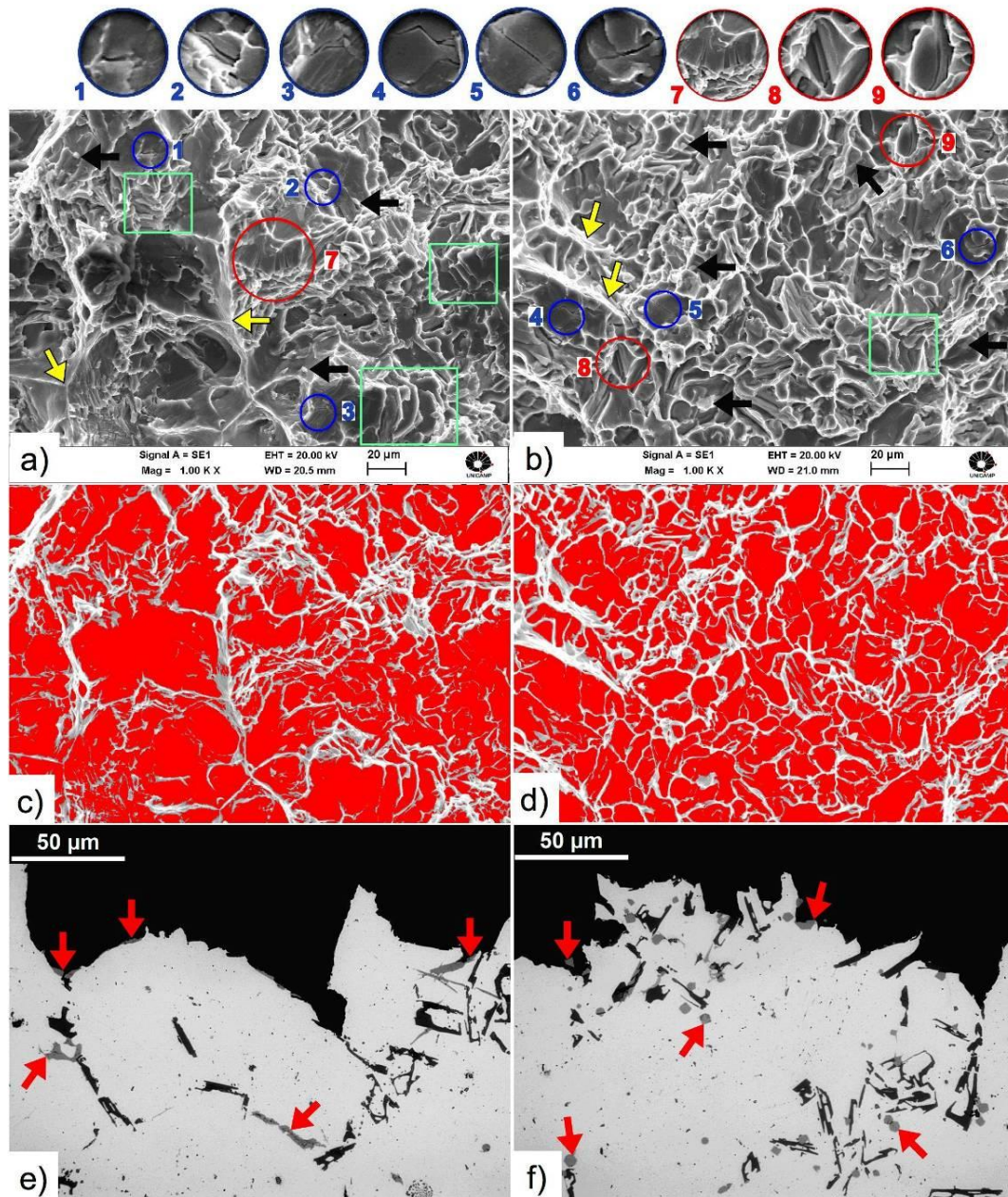
Figure 7: Fractured surface (SEM-SE images at the top and filtered binary images, middle) and perpendicular plane from the fractured surface (LOM images, bottom) of the tensile test samples for the Al-5.5Si-5Zn-0.2Mg alloy: after thixoforming at 588 °C (a, c, e); and after SHT at 525 °C for 2.5 h (b, d, f). Precipitates at the fractured surface (black arrows), cleavage facets (yellow arrows), micro-cracks (blue circles), river-like patterns (red circles), terrace-like steps (green rectangles) and Fe-rich precipitates (red arrows) are highlighted. Features inside the circles are zoomed-in at the top of the figure.

The above-described features indicate the occurrence of a transgranular (interdendritic) brittle fracture. However, the fine faceted cleavage observed, with irregular borders in the fracture edges (brighter lines in the SEM images of Fig. 7.a/b) characterize a plastic zone formed at the front of the running cracks. The material in the plastic zone consumes part of (often the majority of) the work of fracture by being plastic deformed, generating the observed discontinuous interface, as observed by MÖSER *et al.* [36].The partially plastic behavior observed is in agreement with the elongation data shown in Table 3. Thus, it is assumed that both TF and SHT conditions present a hybrid (predominantly brittle) fracture mechanism.

The binary filtered images of the fractured surfaces (Fig. 7.c/d) show rounder and finer fractured structures for the SHT condition when compared to the larger and more faceted edges observed for the TF condition. This difference indicates the tendency to form fractured structures closer to dimples for the SHT sample. Furthermore, there is a visible morphological transition of the Fe-rich particles (red arrows) from

acicular (Fig. 7.e) to platelet-like and rounder shape (Fig. 7.f) due to the application of SHT. The rounder morphology of both the fractured edges and Fe-rich particles can have contributed to the transition to a more ductile fracture for the SHT condition when compared to the TF alloy (as seen before in Table 3 and Fig. 6).

3.3 Effect of the SHT on the Zinc Distribution

The element Zn is associated with the rise in the tensile strength and hardness due to solid solution strengthening in Al alloys as attested by ALEMDAG et al. [37]. Then, in an attempt to explain the optimum mechanical strength and hardness presented by the SHT condition, the displacement and distribution of Zn along the several steps of the processing route was performed. Figures 8 and 9 show micrographs of the Al5.5Si5Zn0.2Mg alloy obtained via B&W LOM (1st column, left), SEM-BSD (2nd column), SEM-EDS mapping for element Zn (3rd column) and SEM-EDS punctual chemical analysis (in wt%) for Zn along adjacent globules (4th column, right).

The temperatures for the chemical distribution analysis were chosen based on the CALPHAD simulation for the alloy (Fig. 2) and are described as follows: In Fig. 8 the conditions analyzed are(a) room temperature or as cast; (b) partially melted at 440 °C, in which the alloy is still completely solid; (c) PM at 540 °C, in which Mg_2Si and $Al_8FeMg_3Si_6$ particles are supposed to be completely molten ($f_s = 0.94$); (d) PM at 575 °C, above the eutectic knee, in which Si eutectic and AlFeSi-β phaseare completely molten ($f_s = 0.55$) and (e) 588 °C, the working temperature ($f_s = 0.40$). In Fig. 9 the conditions are (a)after thixoforging at 588 °C, in order to analyze the effects of heat associated to strain (metal forming), and after thixoforging + SHT at 525 °C for 1 (b), 2.5 (c), 3 (d) and 6 h (e), to analyze the combined effects of heat, strain and facilitated diffusion. According to the simulation in the Scheil condition (Fig. 2), at 525 °C it is expected that the alloy presents Al_{FCC} + Si + $Al_8FeMg_3Si_6$ phases and a small amount of liquid (fs = 0.96) due to the melting of the Mg_2Si phase.

For the as cast condition (Fig. 8.a), zinc is concentrated at the eutectic phase and gradually dispersed in smaller contents to the dendrite center. The SEM-BSD image indicates the Zn-rich zone as being brighter which is also shown by the SEM-EDS map (green areas) and punctual EDS analysis. According to the CALPHAD simulation (Fig. 1), it is expected that Zn and Mg combine in the form of the $MgZn_2$ phase below 150 °C. Furthermore, a tendency of Zn-rich nano-precipitates to concentrate along coarser phases (such as $Al_{20}Cu_2Mn_3$-T and $Al_{18}Mg_3Cr_2$-E) at room temperature was observed for Al-Zn-Mg alloys by several authors as AFIFI et al. [38], LUTZ et al. [39], and AFIFI et al. [41].

For partial melting ranging from 440 to 588 °C (Fig. 8.b-e), Zn follows the movement of the second phase, and its concentration is diminished inside the globules. This is a surprising result, since according to the CALPHAD simulation Zn was expected to diffuse along the matrix with the rise in temperature. The kinetic effect of rapid heating (50 °C/min) may have retarded Zn dissolution, pushing it to higher temperatures when compared to the near-equilibrium simulated condition.

After thixoforging (Fig. 9.a), Zn is spread throughout the matrix, as a result of the dislocation motion, which acts to distribute the solutes like Zn, Mg, Mn, Cr and Cu. Dislocations are generated and move as a result of the plastic strain suffered by the large amount of solid fraction at the end of thixoforming due to the rapid heat transfer from the slurry to the dies as shown by ZHANG et al. [42].

The SHT (Fig. 9.b-d) promotes homogeneous distribution of Zn from 1 to 3 h. Zn-rich nano-particles are known to precipitate along dislocations as a recovery promoter mechanism enabled for temperature: precipitation leads to the accumulation of dislocations followed by annihilation of opposite sign dislocation loops as shown by GUO et al. [40]. Zinc in solid solution as seen for 1 to 3 h of SHT is in agreement with the CALPHAD simulation. TEM observations in at GUO et al. [9] and BUHA et al. [43] indicate the presence of GP zones inside the primary phase grains presenting embryos of $MgZn_2$, which increased the mechanical strength of alloys from the 7xxx series after metal forming and SHT. This occurs because GP zones are known to hinder dislocation movement due to the generation of comprehensive strain by substituting Zn for Al atoms to form these solute agglomerates as presented in BAI, et al. [17] and ZHU et al. [27]. Previous papers, ZHU et al. [26] and ZHU et al. [27], also associated the presence of Zn atoms solubilized in the Al matrix with increased partitioning of other secondary elements, such as Mg, Si, and Cu, from the Al matrix into solute clusters and GP zones. These results may be an explanation for the increase in yield stress and ultimate tensile stress seen for the studied alloy after thixoforming + SHT.

Finally, after 6 hot SHT (Fig. 9.e), Zn segregates to the eutectic again. The concentration of Zn at the eutectic in Fig. 9.e cannot be a result of kinetic effects (as supposed for the conditions in Figs. 8.b-e), since the influence of kinetics would be minimized or even suppressed after a long period of SHT. The preferential formation of Zn-rich solute clusters and/or GP zones near and/or in eutectic loci may explain this concentration. These nano-sized structures may have formed preferentially in the eutectic due to (a) the high concentration of its constituent elements (Zn, Mg, Cu, Si, etc.), (b) the presence of phases with lower melting temperatures when compared to the primary phase, resulting in a lesser thermodynamic stability than the Al-

matrix and (c) facilitated diffusion in relation to the primary phase due to the partial melting of the eutectic ($f_S = 0.96$ at 525 °C according to the CALPHAD simulation).
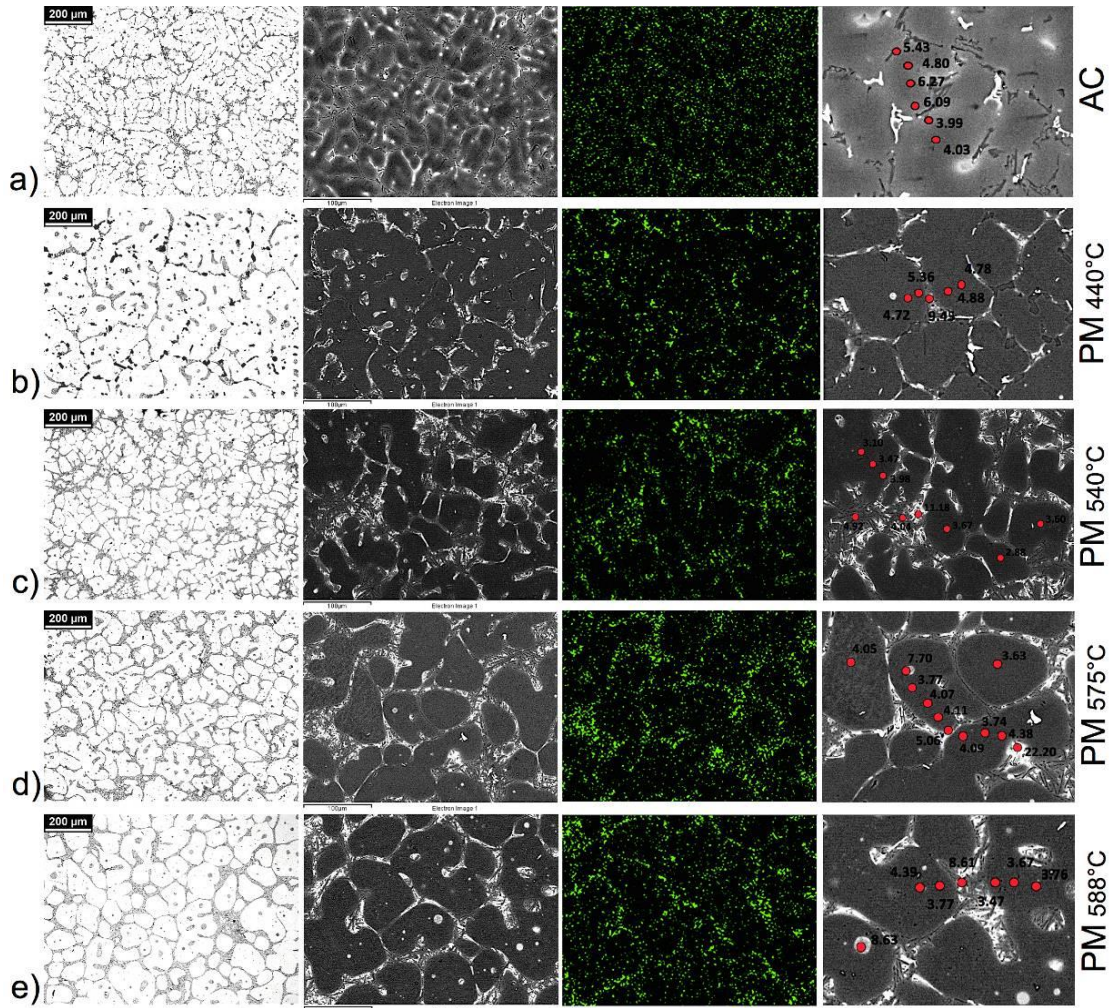

Figure 8: Micrographs of the Al5.5Si5Zn0.2Mg alloy obtained via B&W LOM (1st column, left), SEM-BSD (2nd column), SEM-EDS mapping for element Zn (3rd column) and SEM-EDS punctual chemical analysis (red dots, in wt%) for Zn along adjacent globules (4th column, right) at (a) room temperature – as cast; (b) 440 °C – alloy still completely solid; (c) 540 °C – $f_s = 0.94$, Mg$_2$Si and Al$_8$FeMg$_3$Si$_6$ particles are completely molten; (d) 575 °C – $f_s = 0.55$, above the eutectic knee, Si eutectic and AlFeSi-β are completely molten and (e) 588 °C – $f_s = 0.40$, working temperature.
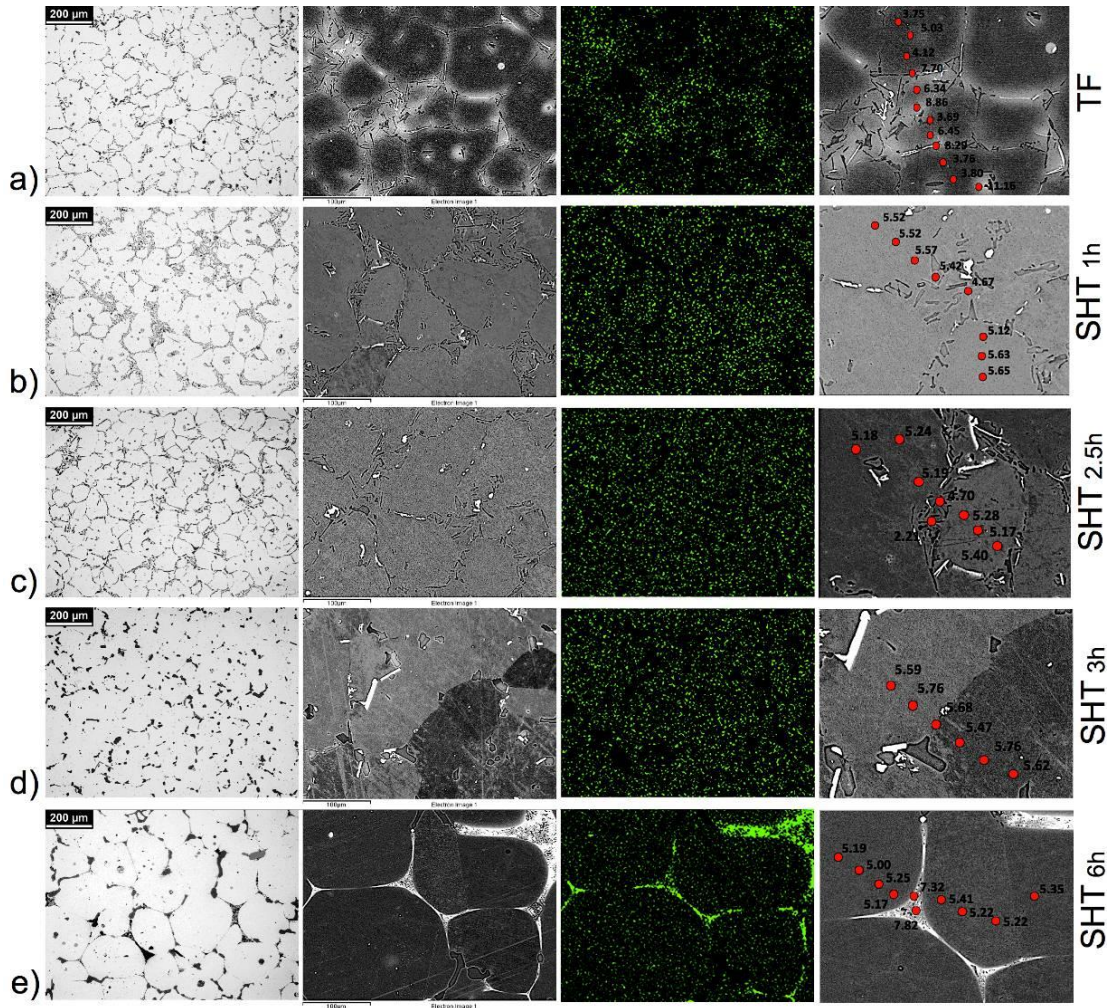
Figure 9: Micrographs of the Al5.5Si5Zn0.2Mg alloy obtained via B&W LOM (1st column, left), SEM-BSD (2nd column), SEM-EDS mapping for element Zn (3rd column) and SEM-EDS punctual chemical analysis (red dots, in wt%) for Zn along adjacent globules (4th column, right) after (a) thixoforging at 588 °C, f_s = 0.40 – effects of temperature and strain; thixoforging + SHT 525 °C, f_s = 0.96, for 1 (b), 2.5 (c), 3 (d) and 6 h (e) – effects of temperature, strain and facilitated diffusion.

Hardness Vickers measurements were performed for all the conditions analyzed in Figs. 8 and 9and are presented (average ± standard deviation) in Table 4.By confronting the Zn spatial distribution with the HV values, it can be seen that the hardness decreases with the progressive concentration of Zn at the secondary phase: parting from the as cast condition (Fig. 8.a), with fine intricate dendritic structure and thus with more dispersed Zn, the alloy presented HV = 72×10^{-1}kgf/s, changing to HV = $61\text{-}66 \times 10^{-1}$kgf/s with the progressive Zn concentration to secondary phase loci heterogeneously distributed along the structure (Fig. 8.b-e). After thixoforging (Fig. 9.a), the hardness increased to HV = 75×10^{-1}kgf/s, in agreement with the homogeneous Zn dispersion along the matrix, a behavior maintained after 1h of SHT (Fig. 9.b).

For 2.5 h of SHT (Fig. 9.c), the hardness reaches its maximum value (HV = 82×10^{-1}kgf/s). In addition to the Zn dispersion, at this condition Si crystals achieve the optimum degree of spheroidization (as seen in section 3.1), which also contributes to the hardening effect. After 3 h at 525 °C (Fig. 9.d/e), grain coarsening leads to another decrease in hardness (HV = $73\text{-}74 \times 10^{-1}$kgf/s). For the last condition (6 h) the standard deviation associated with hardness rises considerably due to the presence of coarser Si crystals (substantially harder than the matrix) limited to sparse regions of the measurement area.

Table 4: Hardness Vickers (average ± standard deviation) for the Al5.5Si5Zn0.2Mg alloy corresponding to each condition of temperature (T) and holding time (t) shown in Figs. 8 and 9.

CONDITION	T(°C)	T (h)	HV (10^{-1}kgf/s)
AC	25	-	72 ± 2
PM	440	-	61 ± 1
	540	-	61 ± 2
	575	-	62 ± 2
	588	-	66 ± 2
TF	588	-	75 ± 2
SHT	525	1	73 ± 3
		2,5	82 ± 2
		3	73 ± 1
		6	74 ± 6

3.4 The Association of Zinc to Other Alloying Elements

In order to investigate the association of Zn with other secondary elements that could explain the behavior of the above-discussed Zn movement and position in the matrix along the processing steps, the chemical distribution of other secondary elements present in the alloy was also performed. Figure 10 presents micrographs of the Al-5.5Si-5Zn-0.2Mg alloy obtained via SEM-SE (1st column, left) and SEM-EDS mapping for the elements Zn, Si, Mg, Fe, Mn and Cu (further columns) at the conditions: as cast (a); partially melted at 588 °C (b); after thixoforging at 588 °C (c); after thixoforging + SHT at 525 °C for 2.5 h (d) and 6 h (e).

Silicon is located around the primary phase grains at all the analyzed conditions, which is expected considering Si is the main constituent of the eutectic and that the Al-α phase presents low Si content. Iron is also found distributed along the eutectic, however concentrated to fewer regions than seen for Si, due to the lower content of Fe in the alloy when compared to Si. Eutectic phases containing Si and Fe are the only that remain visible via EDS analysis (Fig. 10) at all the tested conditions, indicating their thermodynamic stability along the studied temperature range and strain applied to the alloy. This result is in agreement with the CALPHAD simulation (Figs. 1 and 2), which predicted that the Si-rich eutectic and the AlFeSi-β phase should be the first to form after the Al-α phase during solidification. In addition to the patterns of Fig. 10, the Fe-rich phase can be seen in the B&W micrographs of Figs. 5, 7, 8 and 9, where it appears as light grey particles in the eutectic (in contrast to the dark grey Si crystals).

A certain degree of correspondence between the Fe and Mn distribution patterns at 525 °C can be seen in Fig. 10 (SHT for 2.5 and 6 h), indicating the precipitation of Fe,Mn-rich compounds during SHT. For 2.5 h of SHT coarser platelet-like Fe-(Mn,Si)-rich particles are observed instead of the former acicular shape presented in the thixoformed condition, contributing to the achievement of the higher strength observed for this condition, since they minimize crack generation and propagation. The morphological change of Fe-rich particles can also be observed in Figs. 5, 7, 8and 9 (light grey particles in the eutectic). The iron phases are considered the most harmful in Al-Si alloys because of their deleterious effects on ductility and corrosion resistance. The studied alloy presents 0.24 wt.%Fe, which is far below the maximum recommended limit of 0.6-0.7 wt.%, so the role of the Fe-rich particles on the mechanical performance of the alloy should be negligible when compared to other microstructural features, such as the primary phase, Si crystals morphology and Zn distribution as presented by ALEMDAG et al. [37].

Magnesium follows a similar distribution pattern as that obtained for Zn. Association of Mg and Si (Mg$_2$Si) is predicted by the Scheil simulation (Fig. 2) below 522 °C. The association of Mg, Si and Fe is also expected in the form of the Al$_8$FeMg$_3$Si$_6$ compound below 529 °C. The SHT at 525 °C for intermediate holding times (1 to 3 h) possibly facilitated the dissolution of Mg-containing agglomerates with the consequent dispersion of Mg along the matrix. According to LUTZ et al. [39], the dissolution of Al$_{18}$Mg$_3$Cr$_2$-E precipitates during SHT at 470 °C contributed to the homogeneous distribution of the elements Mg and Cr for an Al-4.5Zn-2.5Mg alloy. As discussed for Fig. 9, once in solid solution, Mg can have associated to Zn as GP zones containing embryos of MgZn$_2$ as presented by GUO et al. [9] and XU et al. [44], or clusters containing Zn and other secondary elements as observed by ZHU et al. [26], ZHU et al. [27], and GUO et al. [28].

The presence of Zn in Al alloys plays a major role in the partitioning of Mg, Si, and Cu atoms from the Al matrix into solute clusters, GP zones and metastable precipitates, which results in a remarkable age hardening effect when compared to Zn-free alloys as attested by and LIU et al. [29].

An appreciable concentration of Cu in the eutectic region is only seen for 6h of SHT, indicating its association to other secondary elements, as discussed above for Mg. The precipitation of hard Al-, Mg- and Cu-rich particles around primary-phase grains is beneficial to the corrosion resistance of Al-Cu-Mg alloys as shown by CASATI et al. [45]. Furthermore, fine Al$_2$Cu particles formed after ageing are associated to a rise

in the hardness of the thixoformed and T6 heat-treated A380 alloy as presented by GECU *et al.* [2].The presence of Cu in the eutectic is also associated to an increase in hardness by refining the Mg_2Si precipitates as shown by LUTZ *et al*. [39]. On the other hand, higher SHT temperature could lead to the incipient melting of the Al_2Cu phase in Al-Si-Cu and Al-Si-Cu-Mg alloys. This phenomenon was observed for temperatures of approx. 540 °C (the temperature used in this work is 525 °C) and resulted in grain boundary weakening, facilitating brittle intergrannular fracture as observed by GAO *et al.* [35].

The concentration of Zn-, Mg- and Cu in the eutectic after 6 h of SHT is not desired, since a supersaturated matrix with these elements is the main goal of the SHT in order to achieve better precipitation hardening after aging as presented by CASATI *et al.* [45]. For this reason and the other aspects discussed along this work, 2.5 h is considered the optimum holding time for the SHT applied to the studied alloy.
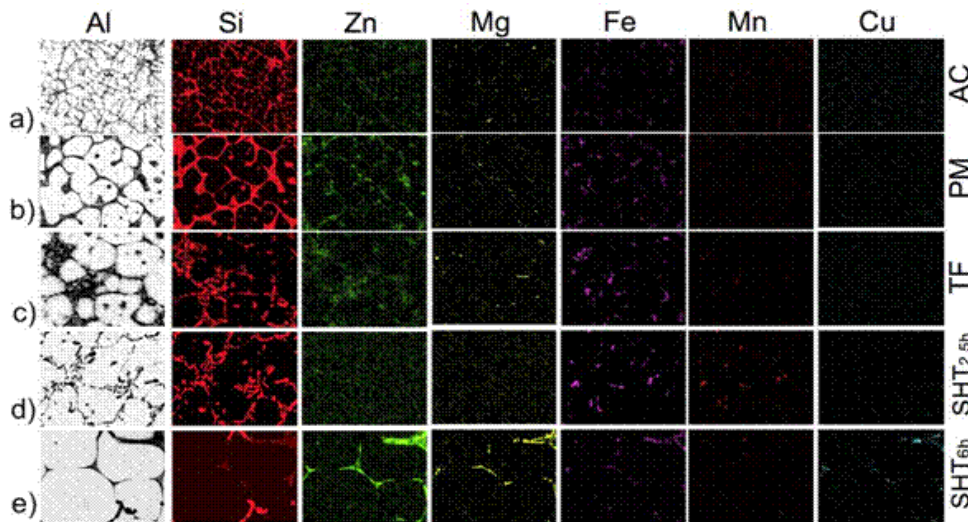

Figure 10: Micrographs of the Al-5.5Si-5Zn-0.2Mg alloy obtained via SEM-BSD (1st column, left) and SEM-EDS mapping for elements Si, Zn, Mg, Fe, Mn and Cu (further columns) at the conditions: as cast (a); partial melting at 588 °C (b); after thixoforging at 588 °C (c); after thixoforging + SHT for 2.5 h (d) and 6 h (e) at 525 °C.

4. CONCLUSION

The solution heat treatment at 525 °C for 2.5 h applied after open die thixoforging at 588 °C (f_s = 0.40, strain = 0.5) to the Al-5.5wt%Si-5wt%Zn-0.2wt%Mg alloy showed to be adequate considering the spheroidization of eutectic Si crystals, the formation of Fe, Mn-rich platelets-like particles in the eutectic phase, the Mg dissolution from the Mg_2Si conglomerates and the homogeneous Zn diffusion along the entire part.

The possible formation of solute clusters and GP zones containing Zn, Mg, Si and Cu was enabled due to the dissolution and diffusion of secondary elements during SHT for 2.5 h, which caused the increase of the alloy's mechanical strength. Larger Si crystals and the homogeneous spatial spread of Zn resulted in the hardness increase of the SHT for 2.5 h alloy when compared to the thixoformed and other SHT conditions.

5. ACKNOWLEDGMENTS

6. REFERENCES

[1] KILICLI, V., AKAR, N., ERDOGAN, M., *et al.* "Tensile fracture behavior of AA7075 alloy produced by thixocasting", https://doi.org/10.1016/S1003-6326(16)64223-1. *Transactions of Nonferrous Metals Society of China*, v. 26, pp.1222−1231, 2016.

[2] GECU, R., ACAR, S., KISASOZ, A., *et al.* "Influence of T6 heat treatment on A356 and A380 aluminium alloys manufactured by thixoforging combined with low superheat casting", https://doi.org/10.1016/S1003-6326(18)64672-2. *Transactions of Nonferrous Metals Society of China*, v. 28, pp. 385−392, 2018.

[3] CURLE, U.A., "Semi-solid near-net shape rheocasting of heat treatable wrought aluminum alloys", https://doi.org/10.1016/S1003-6326(09)60364-2. *Transactions of Nonferrous Metals Society of China*, v. 20, pp. 1719-1724, 2010.

[4] BINESH, B., AGHAIE-KHAFRI, M., "RUE-based semi-solid processing: Microstructure evolution and effective parameters", https://doi.org/10.1016/j.matdes.2016.01.117. *Materials & Design*, v. 95, pp. 268–286, 2016.

[5] ROGAL, Ł., DUTKIEWICZ, J., ATKINSON, H.V., *et al.* "Characterization of semi-solid processing of aluminium alloy 7075 with Sc and Zr additions", https://doi.org/10.1016/j.msea.2013.04.078. *Materials Science and Engineering A*, v. 580, pp. 362–373, 2013.

[6] CHEN, G., JIANG, J., DU, Z., *et al.* "Formation of Fine Spheroidal Microstructure of Semi-Solid Al-Zn-Mg-Cu Alloy by Hyperthermally and Subsequent Isothermally Reheating", https://doi.org/10.1016/j.jmst.2013.05.008. *Journal of Materials Science & Technol*ogy, v.29-10, pp. 979-982, 2013.

[7] ZOQUI, E.J., "Alloys for semisolid processing", in: McGeough J. (Ed.), Compreensive Materials Processing. https://doi.org/10.1016/B978-0-08-096532-1.00520-3. Elsevier Ltd, v. 5, pp. 163-190, 2014

[8] SHIN, S., LIM, K., PARK, I., "Effects of high Zn content on the microstructure and mechanical properties of Al–Zn–Cu gravity-cast alloys", https://doi.org/10.1016/j.msea.2016.09.022. *Materials Science and Engineering A*, v. 679, pp. 340–349, 2017.

[9] GUO, W., GUO, J., WANG, J., *et al.* "Evolution of precipitate microstructure during stress aging of an Al–Zn–Mg–Cu alloy", http://dx.doi.org/10.1016/j.msea.2015.03.047. *Materials Science and Engineering A*, v. 634, pp. 167–175, 2015.

[10] LIN, Y.C., JIANG, Y., CHEN, X., *et al.* "Effect of creep-aging on precipitates of 7075 aluminum alloy", http://dx.doi.org/10.1016/j.msea.2013.09.045. *Materials Science and Engineering A*, v. 588, pp. 347–356, 2013.

[11] LIN, Y.C., ZHANG, J., LIU, G., *et al.* "Effects of pre-treatments on aging precipitates and corrosion resistance of a creep-aged Al–Zn–Mg–Cu alloy", http://dx.doi.org/10.1016/j.matdes.2015.06.029. *Materials & Design*, v.83, pp. 866–875, 2015.

[12] CHAO, L., HE, Y., HENG, L., *et al.* "Dependence of creep age formability on initial temper of an Al-Zn-Mg-Cu alloy", http://dx.doi.org/10.1016/j.cja.2016.04.022. *Chinese Journal of Aeronaut*ics, v. 29-5, pp. 1445–1454, 2016.

[13] LEI, C., LI, H., ZHENG, G.W., *et al.* "Thermal-mechanical loading sequences related creep aging behaviors of 7050 aluminum alloy", https://doi.org/10.1016/j.jallcom.2017.10.035. *Journal of Alloy and Compounds*, v.731, pp. 90-99, 2018.

[14] WEN, K., FAN, Y., WANG, G., *et al.* "Aging behavior and precipitate characterization of a high Zn-containing Al-Zn-Mg-Cu alloy with various tempers", http://dx.doi.org/10.1016/j.matdes.2016.03.150. *Materials & Design*, v.101, pp. 16–23, 2016.

[15] ABD EL-SALAM, F., MOSTAFA, M.M., WAHAB, L.A., *et al.* "Enhanced creep parameters of Al–Zn alloy induced by cyclic stress reduction", https://doi.org/10.1016/j.msea.2007.04.023. *Materials Science and Engineering A*, v. 474, pp. 230–235, 2008.

[16] NADA, R.H., ABD EL-SALAM, F., WAHAB, L.A., *et al.* "Frequency and temperature dependence on the creep characteristics of Al-5 wt.% Zn alloy", https://doi.org/10.1016/j.msea.2012.02.072. *Materials Science and Engineering A*, v. 543, pp. 180–184, 2012.

[17] BAI, P.C., LIU, F., HOU, X.H., *et al.* "Experimental examination of strain field within GP zone in an Al–Zn–Mg–Cu alloy", http://dx.doi.org/10.1016/j.physb.2012.07.048. *Physica B*, v. 407, pp. 4466–4469, 2012.

[18] PRONI, C.T.W., DE PAULA, L.C., TORRES, L.V., *et al.* "Evaluation of Al-5wt%Si-5wt%Zn as Raw Material for Semisolid Forming", https://doi.org/10.4028/www.scientific.net/SSP.285.339. *Solid State Phenomena*, v. 285, pp. 339–344, 2019.

[19] PRONI, C.T.W., BROLLO, G.L., ZOQUI, E.J., "A Comparison of the Use of Ultrasonic Melt Treatment and Mechanical Vibration in the Manufacture of Al5Si5Zn Alloy Feedstock for Thixoforming", https://doi.org/10.1007/s11663-019-01741-7. *Metallurgical and Materials Transactions B*, v. 51B, pp. 306-317, 2020.

[20] DANTAS, A.V.R, BROLLO, G.L., TAMAYO, D.V., *et al.* "Thixoforming of an Al-Si-Zn-Mg Alloy - Thermodynamic Characterization, Microstructural Evolution and Rheological Behavior", https://doi.org/10.1590/1980-5373-mr-2020-0313. *Materials Research*, v.24-2, e20200313, 2021.

[21] SHU, W.X., HOU, L.G., ZHANG, C., *et al.* "Tailored Mg and Cu contents affecting the microstructures and mechanical properties of high-strength Al–Zn–Mg–Cu alloys", https://doi.org/10.1016/j.msea.2016.01.039. *Materials Science and Engineering A*, v. 657, pp. 269–283, 2016.

[22] PRIYA, P., JOHNSON, D.R., KRANE, M.J.M., "Precipitation during cooling of 7XXX aluminum alloys", https://doi.org/10.1016/j.commatsci.2017.08.008. *Computational Materials Science*, v. 139, pp. 273–284, 2017.

[23] AFSHARI, B.M., MIRJAVADI, S.S., DOLATABAD, Y.A., et al. "Effects of pre-deformation on microstructure and tensile properties of Al−Zn−Mg−Cu alloy produced by modified strain induced melt activation", https://doi.org/10.1016/S1003-6326(16)64349-2. Transactions of Nonferrous Metals Society of China, v. 26, pp. 2283−2295, 2016.

[24] ROMETSCH, P.A., ZHANG, Y., KNIGHT, S., "Heat treatment of 7xxx series aluminium alloys - Some recent developments", https://doi.org/10.1016/S1003-6326(14)63306-9. Transactions of Nonferrous Metals Society of China, v. 24, pp. 2003−2017, 2014.

[25] CHEN, G., JIANG, J., DU, Z., et al. "Formation of Fine Spheroidal Microstructure of Semi-Solid AleZneMgeCu Alloy by Hyperthermally and Subsequent Isothermally Reheating", http://dx.doi.org/10.1016/j.jmst.2013.05.008. Journal of Materials Science & Technology., v. 29, pp. 979-982, 2013.

[26] ZHU, S., LI, Z., YAN, L., et al. "Effects of Zn addition on the age hardening behavior and precipitation evolution of an Al-Mg-Si-Cu alloy", https://doi.org/10.1016/j.matchar.2018.08.051. Materials Characterization, v. 145, pp. 258–267, 2018.

[27] ZHU, S., LI, Z., YAN, L., et al. "Natural aging behavior in pre-aged Al-Mg-Si-Cu alloys with and without Zn addition", https://doi.org/10.1016/j.jallcom.2018.09.244. Journal of Alloy and Compounds, v. 773, pp. 496-502, 2019.

[28] GUO, M.X., LI, G.J., ZHANG, Y.D., et al. "Influence of Zn on the distribution and composition of heterogeneous solute-rich features in peak aged Al-Mg-Si-Cu alloys", https://doi.org/10.1016/j.scriptamat.2018.09.004. Scripta Materialia, v. 159, pp. 5–8, 2019.

[29] LIU, D., ATKINSON, H.V., JONES, H., "Thermodynamic prediction of thixoformability in alloys based on the Al–Si–Cu and Al–Si–Cu–Mg systems", https://doi.org/10.1016/j.actamat.2005.04.028. Acta Materialia, v. 53, pp. 3807–3819, 2005.

[30] PRONI, C.T.W., ZOQUI, E.J.: "The effect of heating rate on the microstructural breakdown required for thixoformability", https://doi.org/10.3139/146.111472. Interntional Journal of Materials Research, v. 108-3, pp 228-236, 2017.

[31] ASTM International E384-16. Standard Test Methods for Tension Testing of Metallic Materials, USA, 2016. Last previous edition approved 2016 as E8/E8M − 16. DOI: 10.1520/E0008_E0008M-16A.

[32] ZOQUI, E.J., SHEHATA, M.T., PAES, M., et al. "Morphological evolution of SSM A356 during partial remelting", https://doi.org/10.1016/S0921-5093(01)01401-0. Materials Science and Engineering A, v. 325, pp. 38–53, 2002.

[33] ASTM International E112-13. Standard Test Methods for Determining Average Grain Size. Available online: https://www.astm.org/Standards/E112.htm (accessed on 8 March 2018).

[34] BEROUAL, S., BOUMERZOUG, Z., PAILLARD, P., et al. "Effects of heat treatment and addition of small amounts of Cu and Mg on the microstructure and mechanical properties of Al-Si-Cu and Al- Si-Mg cast alloys", https://doi.org/10.1016/j.jallcom.2018.12.365. Journal of Alloy and Compounds, v. 784, pp. 1026-1035, 2019.

[35] GAO, L., ZHANG, L., GU, XOU J., et al. "Transformation of fracture mode of an Al-Mg-Si-Cu alloy subject to aging treatment", https://doi.org/10.1016/j.msea.2018.08.028. Materials Science and Engineering A, v. 735, pp. 201–207, 2018.

[36] MÖSER, M., "Fractography with the SEM (Failure Analysis)", In: H. Bethge, J. Heydenreich, Microscopy in Solid State Physics, ISBN: 0444989676 9780444989673 0444416854 9780444416858. Elsevier Ltd, pp. 366-385, 1987.

[37] ALEMDAG, Y., BEDERB, M., "Microstructural, mechanical and tribological properties of Al–7Si–(0–5) Zn alloys", https://doi.org/10.1016/j.matdes.2014.06.006.
Materials & Design, v. 63, pp. 159-167, 2014.

[38] AFIFI, M.A., WANG, Y.C., CHENG, X., LI, S., et al. "Strain rate dependence of compressive behavior in an Al-Zn-Mg alloy processed by ECAP", https://doi.org/10.1016/j.jallcom.2019.03.390. Journal of Alloy and Compounds, v. 791, pp. 1079-1087, 2019.

[39] LUTZ, A., MALET, L., DILLE, J., et al. "Effect of Zn on the grain boundary precipitates and resulting alkaline etching of recycled Al-Mg-Si-Cu alloys", https://doi.org/10.1016/j.jallcom.2019.04.259. Journal of Alloy and Compounds, v. 794, pp. 435-442, 2019.

[40] GUO, M.X., DU, J.Q., ZHENG, C.H., et al. "Influence of Zn contents on precipitation and corrosion of Al-Mg-Si-Cu-Zn alloys for automotive applications", https://doi.org/10.1016/j.jallcom.2018.11.146. Journal of Alloy and Compounds, v. 778, pp. 256-270, 2019.

[41] AFIFI, M.A., WANG, Y.C., PEREIRA, P.H.R., et al. "Mechanical properties of an Al-Zn-Mg alloy processed by ECAP and heat treatments", https://doi.org/10.1016/j.jallcom.2018.07.343. Journal of Alloy and Compounds, v. 769, pp. 631-639, 2018.

[42] ZHANG, J., LI, Z., WEN, K., et al. "Simulation of dynamic recrystallization for an Al-Zn-Mg-Cu alloy using cellular automaton", https://doi.org/10.1016/j.pnsc.2019.04.002. Progress in Natural Science: Materials International, v.29-4, pp 477-484, 2019.

[43] BUHA, J., LUMLEY, R.N., CROSKY, A.G., "Secondary ageing in an aluminium alloy 7050", https://doi.org/10.1016/j.msea.2008.02.039. Materials Science and Engineering A, v. 492, pp. 1-10, 2008.

[44] XU, Y., ZHAN, L., MA, Z., *et al.* "Effect of heating rate on creep aging behavior of Al-Cu-Mg alloy", http://dx.doi.org/10.1016/j.msea.2017.02.030. *Materials Science and Engineering A*, v. 688, pp. 488–497, 2017.

[45] CASATI, R., CODURI, M., RICCIO, M., *et al.* "Development of a high strength Al-Zn-Si-Mg-Cu alloy for selective laser melting", https://doi.org/10.1016/j.jallcom.2019.06.123, *Journal of Alloy and Compounds*, v. 801, pp. 243-253, 2019.

ORCID

Gabriela Lujan Brollo   http://orcid.org/0000-0002-0427-9251
Cecília Tereza Weishaupt   http://orcid.org/0000-0001-8607-0066
Eugênio José Zoqui   http://orcid.org/0000-0002-3614-0051